Open access • Journal Article • DOI:10.1016/J.MSEA.2018.07.008

Laser powder bed fusion of Hastelloy X: Effects of hot isostatic pressing and the hot cracking mechanism — Source link

Quanquan Han, Raya Mertens, Maria L. Montero-Sistiaga, Maria L. Montero-Sistiaga ...+6 more authors

Institutions: Cardiff University, Katholieke Universiteit Leuven, Laborelec

Published on: 08 Aug 2018 - Materials Science and Engineering A-structural Materials Properties Microstructure and Processing (Elsevier)

Topics: Hot isostatic pressing, Superalloy, Stress concentration, Hot pressing and Ultimate tensile strength

Elsevier Editorial System(tm) for Materials Science & Engineering A

Manuscript Draft

Manuscript Number:

Title: Selective laser melting of Hastelloy-X: microstructure and mechanical properties

Article Type: Research Paper

Keywords: Selective laser melting, Hastelloy-X, Microstructure, Mechanical properties, Fatigue life

Corresponding Author: Professor Rossitza Setchi, PhD

Corresponding Author's Institution: Cardiff University

First Author: Quanquan Han, PhD

Order of Authors: Quanquan Han, PhD; Raya Mertens; Shoufeng Yang, PhD; Rossitza Setchi, PhD; Maria L Montero-Sistiaga; Kim Vanmeensel, PhD; Brecht Van Hooreweder, PhD; Sam L Evans, PhD

Abstract: Hastelloy-X is the trademark for a nickel-based, high-temperature super-alloy that is increasingly applied in gas turbine engines because of its exceptional combination of oxidation resistance and high-temperature strength. This increased hardness and strength, however, makes the material difficult to form when using traditional manufacturing techniques. Selective laser melting (SLM) is an advanced manufacturing process which offers the ability to manufacture Hastelloy-X using a layer-by-layer manufacturing principle. This paper systematically studies the microstructure and mechanical properties of SLM-fabricated Hastelloy-X, with an emphasis on fatigue performance. The experimental results demonstrated that the optimum scanning speed and hatch spacing were 200 mm/s and 90 μm, respectively, when a relatively low laser power (95 W) was employed; under this optimum condition, a 99.5% relative density was achieved. Due to the difference in solidification rates, the microstructure of the austenite phase that was formed showed different types of grain orientations. The specimens offered a consistent 470 MPa yield strength with a fairly high elongation of 40%. Compared to the fatigue life of comparable materials from CES EduPack, the SLM-manufactured Hastelloy-X was found to offer much higher fatigue life in the relatively lower-cycle range and similar fatigue life in the higher-cycle range.

Cover letter

Dear Editors,

I am pleased to offer our manuscript entitled 'Selective laser melting of Hastelloy-X: microstructure and mechanical properties'. I hope that you will find it of sufficient quality and interest for the readership of the journal.

This paper systematically studies the microstructure and mechanical properties of SLM-fabricated Hastelloy-X, with an emphasis on fatigue performance, which is systematically investigated for the first time in this study. The results are also compared with the data from CES EduPack.

I confirm that the work submitted is original and has not been published before; it is not under consideration for publication anywhere else. Please be advised that colour is to be used in the electronic version only.

Corresponding authors:

Rossitza Setchi, setchi@cardiff.ac.uk, +44(0)2920875720, Cardiff School of Engineering, Cardiff University, Cardiff CF24 3AA, UK

Shoufeng Yang, shoufeng.yang@kuleuven.be, +32(0)16324999, Department of Mechanical Engineering, KU Leuven, Celestijnenlaan 300B, box 2420, Heverlee B-3001, Leuven, Belgium

Email addresses for other authors:

Quanquan Han, hanq1@cardiff.ac.uk

Raya Mertens, raya.mertens@kuleuven.be

Maria L. Montero-Sistiaga, maria.montero@kuleuven.be

Kim Vanmeensel, kim.vanmeensel@kuleuven.be

Brecht Van Hooreweder, brecht.vanhooreweder@kuleuven.be

Sam L. Evans, EvansSL6@cardiff.ac.uk

Best regards,

Professor Rossi Setchi

Director, Mechanics, Materials and Advanced Manufacturing Research Theme

Cardiff University, UK

Selective laser melting of Hastelloy-X: microstructure and mechanical properties

Quanquan Han[a], Raya Mertens[b], Shoufeng Yang[b]*, Rossitza Setchi[a]*, Maria L. Montero-Sistiaga[c], Kim Vanmeensel[c], Brecht Van Hooreweder[b], Sam L. Evans[a]

[a] Cardiff School of Engineering, Cardiff University, Cardiff CF24 3AA, UK

[b]Department of Mechanical Engineering, KU Leuven, Celestijnenlaan 300B, box 2420, Heverlee B-3001, Leuven, Belgium

[c]Department of Materials Engineering, KU Leuven, Kasteelpark Arenberg 44, box 2450, Heverlee B-3001, Belgium

Abstract

Hastelloy-X is the trademark for a nickel-based, high-temperature super-alloy that is increasingly applied in gas turbine engines because of its exceptional combination of oxidation resistance and high-temperature strength. This increased hardness and strength, however, makes the material difficult to form when using traditional manufacturing techniques. Selective laser melting (SLM) is an advanced manufacturing process which offers the ability to manufacture Hastelloy-X using a layer-by-layer manufacturing principle. This paper systematically studies the microstructure and mechanical properties of SLM-fabricated Hastelloy-X, with an emphasis on fatigue performance. The experimental results demonstrated that the optimum scanning speed and hatch spacing were 200 mm/s and 90 µm, respectively, when a relatively low laser power (95 W) was employed; under this optimum condition, a 99.5% relative density was achieved. Due to the difference in solidification rates, the microstructure of the austenite phase that was formed showed different types of grain orientations. The specimens offered a consistent 470 MPa yield strength with a fairly high elongation of 40%. Compared to the fatigue life of comparable materials from CES EduPack, the SLM-manufactured Hastelloy-X was found to offer much higher fatigue life in the relatively lower-cycle range and similar fatigue life in the higher-cycle range.

Keywords: Selective laser melting, Hastelloy-X, Microstructure, Mechanical properties, Fatigue life

1. Introduction

Hastelloy-X is a solid-solution-strengthened, nickel-based super-alloy that has been widely applied in gas turbine engines because of its exceptional combination of oxidation resistance, formability and high-temperature strength [1,2]. Compared to other nickel-based alloys such as In718 and In625, Hastelloy-X is resistant to stress-strain cracking in petrochemical applications and offers good ductility, even at 1200°C. Because of Hastelloy-X's increased hardness and tensile strength, however, fabricating the customised engineering parts used in the aerospace and marine domains is a challenge when using traditional manufacturing techniques [3]. Selective laser melting (SLM) is an additive manufacturing process in which metallic powder is selectively melted layer by layer using a high-power laser [4,5]; this process thereby offers the ability to fabricate customised Hastelloy-X engineering parts.

One of the main issues in SLM of Hastelloy-X lies in the thermal induced residual stress and microcracking; some nickel-based super-alloys have been found to be particularly susceptible to microcracking when processed using SLM [6–9]. Several recent studies have focused on the microcrack minimisation in SLM of Hastelloy-X. For instance, Tomus et al. [8] have investigated the effects of minor alloying elements (i.e. Si and Mn) on the crack susceptibility of Hastelloy-X during SLM. The authors found that an alloy with a high Si + Mn content resulted in more microcracks than one with a low Si + Mn content. Their latest research considers two primary factors that control crack formation and propagation: (i) internal strain accumulation due to the thermal cycling and (ii) crack formation and propagation during solidification, which is known as 'hot tearing' and is dependent on chemical composition [10]. Harrison et al. [3] studied the reduction of microcracks in Hastelloy-X by a fundamental

alloy design method; their study found that the alloy's resistance to cracking can be improved by increasing the concentrations of substitutional solid solution strengthening atoms.

A few studies have investigated the mechanical properties and microstructure of SLM-fabricated Hastelloy-X. For example, Tomus et al. [11] investigated the influence of post-heat treatment on the anisotropy of mechanical behaviour and the micro-structure of SLM-fabricated Hastelloy-X and found that the yield strength drastically decreased (by 200 Mpa), while a steady increase (by 10%) of elongation until failure was observed following the heat treatment and/or hot isostatic pressing. Etter et al. [12] studied reductions in mechanical anisotropy through high-temperature heat treatment of SLM-processed Hastelloy-X and found that the anisotropy was observed in the Young's modulus, with lower values measured parallel to the build-up direction when different scanning strategies were employed. After heat treatment, the differences between the scanning strategies were nearly eliminated and the anisotropy of the modulus was greatly reduced. Tian et al. [13] investigated the influences of SLM-process parameters on the surface roughness of Hastelloy-X; they found that the large overlap induced by small hatch distances promoted the attachment of particles on the surface, which in turn increased the surface roughness. For inclined surfaces, the roughness of the up-skin surfaces was virtually unaffected by various scanning powers and speeds, while the roughness of the down-skin surfaces increased with laser power and decreased with scanning speed. Wang [14] studied the tensile and fatigue performances of SLM-fabricated Hastelloy-X using an EOS M270 machine with a relatively high laser power (200 W); because only one fatigue sample was used in each level of applied load, however, the fatigue life might not have been representative in that study; the author did not analyse the fatigue-fracture characteristics in detail.

Accordingly, the aim of the present study was to determine the optimum

SLM parameters (scanning speed and hatch spacing) to produce minimum porosity and cracking in Hastelloy-X components when a relatively low laser power (95 W) is used. This study also investigated the microstructure and mechanical properties of the as-fabricated samples with an emphasis on the fatigue behaviour, which was systematically examined for the first time in this study.

2. Material and procedure

2.1. Material

The Hastelloy-X powder used in this study was obtained from Concept Laser GmbH with a chemical composition (wt.%) of 23Cr-20Fe-10Mo-2.5Co-1Si-1W-bal.Ni. Fig. 1 shows the particle morphology and size of the raw material; the particles were observed to be fairly spherical with an average particle size of 35 µm.

<insert Figure 1>

2.2. The selective laser melting process

A Concept Laser M1 machine equipped with a 100 W fibre laser was employed to manufacture the specimens. Prior to the fabrication of the tensile and fatigue specimens, a set of cubic samples (10 x 10 x 10 mm^3) was manufactured under different conditions in order to determine the optimum scanning speed and hatch spacing. The process parameters that were used are shown in Table 1. The optimum parameters that were obtained were employed to manufacture tensile and fatigue specimens for use in the remainder of the study.

<insert Table 1>

2.3. Material characterisation techniques

The relative density of the as-fabricated cubic samples was measured by

the Archimedes method in order to determine the optimum scanning speed hatch spacing. The four samples with the highest relative densities were then sectioned and polished prior to optical microscopy (OM) and scanning electron microscopy (SEM) observations. For the microstructure analysis, the polished samples were electrochemically etched using oxalic acid for 10 s to reveal molten pool boundaries and solidification microstructures. The crystallographic orientation of the samples was investigated using electron backscattered diffraction (EBSD), which was performed on an FEI Nova NanoSEM 450 instrument equipped with a TSL/EDAX system. Phase identification of the samples was performed using x-ray diffraction (XRD) with Co kα (λ = 1.789 Å) radiation at 35 kV and 40 mA in continuous-scan mode. In addition to phase identification, the XRD data can also be used to determine if the cubic crystal structure is body-centred cubic (BCC) or face-centred cubic (FCC). The indicator r that was used can be expressed as:

$$r = \frac{sin^2\theta_A}{sin^2\theta_B} \quad (1)$$

where θ_A and θ_B represent two diffracting angles associated with the principal diffracting planes, respectively. An r value of 0.5 generally suggests a BCC crystal structure, while a value of 0.75 implies an FCC crystal structure.

The tensile tests were performed using an Instron 4505 testing machine with a strain rate of 1.5 mm/min at room temperature. The yield strength obtained from the tensile tests was used to determine the stresses that would be employed in the fatigue tests that followed; five levels of stress (three samples for each level) were used in the fatigue tests. The fatigue tests were conducted using an MTS 858 Mini Bionix II testing machine with a maximum applied load of 20 KN at room temperature; the frequency was set to 10 HZ, and the stress ratio (R) was maintained at 0.1, which was the ratio of minimum stress to maximum stress applied during the fatigue testing.

2.4. Hypotheses

Two hypotheses were tested in this study:

i. The relative density may increase with an increase in the scanning speed and laser-energy density until the optimum values are attained; the relative density will then decrease when the scanning speed and laser-energy density exceed the optimum values Laser-energy density is expressed as: $\varepsilon = {}^{P}/_{vth}$, where P is the laser power, v, t and h represent the scanning speed, layer thickness and hatch spacing, respectively.

ii. The different solidification rates that are induced by temperature gradient may result in the formation of austenite phase with different grain orientations.

iii. The microcracks that form may have the least influence on both tensile and fatigue performances when the specimens are fabricated vertically.

3. Results

3.1. Relative density

The relative density of the as-fabricated cubic samples with respect to the scanning speed and hatch spacing are shown in Fig. 2. When the hatch spacing was maintained at 60 µm, the relative density measurements increased with an increase in scanning speed until 500 mm/s, which contributed to a relative density of 99%. The relative density then decreased with further increase in scanning speed; a relatively low density measurement of 97.8% was associated with a scanning speed of 800 mm/s, which can be explained by the change in the laser-energy density. A combination of low scanning speed and small hatch spacing generally led to a dramatic increase in laser-energy density, which may cause the laser's working mode to transition from conduction to keyhole mode. A keyhole working mode tends to cause splashing because of the recoil pressure; the splashing, however, could

give rise to high porosity and a relatively low density (97.6%), both of which were obtained at 200 mm/s scanning speed.

<insert Figure 2>

The splashing was reduced and the relative density increased with an increase in scanning speed. But when the scanning speed exceeded the threshold (500 mm/s in the present work), the laser-energy density reduced gradually, and the accumulated heat energy was insufficient to fully melt the Hastelloy-X powder; the relative density thus decreased with a further increase in scanning speed. A similar trend was also observed when the hatch spacing was maintained at 75 μm, although it should be noted that a much lower relative density was observed when the scanning speed exceeded the threshold compared to the hatch spacing of 60 μm. When the hatch spacing was further increased to 90 μm, the relative density was found to have decreased from 99.5% to 95.2%, while the scanning speed increased from 200 mm/s to 800 mm/s. The four samples with the highest relative densities (marked in Fig. 2) were then vertically sectioned to study their defect distributions.

<insert Figure 3>

The porosity and microcrack distribution of the four samples with the highest relative densities are shown in Fig. 3. More specifically, Fig. 3a shows the porosity distribution of the elongated sample fabricated at 200 mm/s scanning speed and 90 μm hatch spacing; a very small number of pores were found to have formed, and no microcracks were observed under this magnification (Fig. 3e). Fig. 3b–d shows typical microstructures when the conditions varied. Both microcracks and pores were generated in these samples, and microcracking seem to be the primary defect in the SLM of Hastelloy-X. The formation of microcracks is believed to be caused by thermal stress, which is induced by the temperature gradient during the laser irradiation; the microcracks are generated when the residual stress is greater

than the ultimate tensile strength during the rapid solidification process. The OM observations confirmed that the optimum scanning speed and hatch spacing in order to fabricate nearly fully dense Hastelloy-X were 200 mm/s and 90 μm, respectively. This parameter combination was employed to fabricate tensile and fatigue specimens for further mechanical-property investigation.

3.2. Phase identification and microstructure

Fig. 4 shows the XRD patterns of the Hastelloy-X powder and the as-fabricated sample fabricated at 200 mm/s scanning speed and 90 μm hatch spacing. A secondary phase was not detected from the diffraction patterns, which suggests that only an austenite single phase was formed following the SLM process. The first two diffraction-angle (2θ) measurements were 51.15° and 59.65°, respectively. An r value of 0.75 was calculated from Eq. (1), which implies that the crystal structure of the austenite phase that formed was FCC.

<insert Figure 4>

Fig. 5 shows the microstructure of the as-fabricated sample under optimum scanning speed and hatch spacing. The molten pool boundary was clearly visible in the vertical section (along the building direction), and a very limited number of pores and microcracks were observed (Fig. 5a). The relatively few defects contributed to the formation of strong metallurgical bonding between two adjacent layers and adjacent hatches; this bonding was expected to improve the material's mechanical properties. Several molten pools were observed to be perpendicular to the rest of the pools in the horizontal section (Fig. 5b); this situation occurred because a 90° rotation angle was employed between two adjacent layers in order to eliminate the chance of scan lines repeating themselves directly on top of one another, thus creating poor material properties.

<insert Figure 5>

Fig. 6 shows SEM micrographs of the as-fabricated samples; these images were useful for further investigation of the microstructure formed in SLM. Figs. 6a and b show the microstructure of the vertical and horizontal sections, respectively, under different magnifications; Fig. 6c shows the microcracks observed in the horizontal section. Specifically, the molten pool boundaries along the building direction were clearly observed in the vertical section (Fig. 6a 1); very fine microstructures with five types of solidification microstructures (I–V) were also observed at the boundary zone (Fig. 6a 2–3). The rapid solidification led to the formation of fine microstructures and the different types of features that were observed were formed because of the different grain orientations.

<insert Figure 6>

Because the XRD analysis confirmed that the phase that had been formed was single phase with an FCC crystal structure, the different solidification microstructures (I–V) observed thus had the microstructure of the austenite phase but differed in grain orientation. Similarly, the molten pool boundaries and different solidification microstructures in the horizontal section were also observed (Fig. 6b 1–3). The average length of the cracks was observed to be 27 μm and a typical microcrack is shown in Fig. 6c 1–3.

Fig. 7 shows an EBSD orientation map of the vertical section fabricated under optimum parameters. The different colours represent the combinations of the Euler angles and grain orientation measured for the FCC crystal lattice in the SLM-fabricated Hastelloy-X. We can see from the figure that the grains that were formed preferentially grew along the energetically favourable <100> and <110> crystal directions. In addition, due to the lack of nucleation barrier to solidification, grains that are produced with crystallographic orientations

identical to those of previously solidified grains can grow epitaxially [15], which explains why some grain axes were larger than the layer thickness (30 μm) that was employed.

<insert Figure 7>

The thermal gradient and cooling rate during the solidification process determined the texture. The four types of solidification microstructures (I–IV) were observed to correspond to the grain orientations shown in Fig. 7a, which confirms the hypothesis that the thermal gradient and cooling rate might result in the formation of the austenite phase with different grain orientations.

3.3. Mechanical properties

3.3.1. Surface topography and tensile performance

The optimum parameters (200 mm/s scanning speed and 90 μm hatch spacing) were employed to fabricate a set of tensile and fatigue specimens (Fig. 8a); the as-fabricated fatigue specimens were polished prior to the fatigue testing (Fig. 8b). Fig. 8c–d shows the top surface topography of the fatigue specimens; the surface was observed to exhibit fairly consistent surface quality, apart from a few 'satellites' that had formed. A satellite, which is a particle that sticks to the surface of the layer that is in contact with the scan track, can be formed by spattering or partial remelting of the powder during the laser-irradiation process. The molten pools were also observed to have an elongated ripple shape; the angle (α) between the ripples and the laser movement direction was in the order of 32° over the majority of the molten pool tail, which can be used to predict the shape of the molten pool.

<insert Figure 8>

Fig. 9 and Table 2 show the tensile-testing results of the as-fabricated specimens. The tensile performances of the four tensile specimens were found

to be very consistent, with a 470 MPa yield strength, 623 MPa ultimate tensile strength, 149 GPa young's modulus and 40% elongation. Necking was observed at the fracture surface following the tensile test. The fairly high elongation (40%) that was observed implies that the samples that were tested showed ductile rather than brittle fracturing. The tensile samples used in this study are shown in Fig. 9b.

<insert Figure 9>

<insert Table 2>

Fig. 10 shows the fracture surface of the Hastelloy-X samples following the tensile test. A typical fracture surface with a few elongated cracks is shown in Fig. 10a 1–3; the very fine dimple structure (a dimple size of < 1 μm) implies a ductile fracture with fairly fine columnar grains formed along the building direction. The elongation ranged up to 40%, although a few microcracks were observed on the fracture surface, which suggests that the influence of microcracks on the elongation of vertically fabricated samples was very limited. A typical crack on the fracture surface is shown in Fig. 10b 1–3; a very fine lamellar structure was observed inside the crack. Compared to the microcracks that were observed before the tensile test (Fig. 6c), the cracks on the fracture surface were found to have opened outwards (i.e. perpendicular to the applied axial load) quite noticeably.

<insert Figure 10>

3.3.2. Fatigue performance

Fig. 11 shows the fatigue performance of the as-fabricated samples under optimal conditions. The S-N curve obtained from the fatigue tests is shown in Fig. 11a; the five-level stresses (250-450 MPa) that were applied were determined based on the yield strength (470 MPa) obtained from the tensile

tests (Fig. 9a). The fatigue life cycles were found to increase with a decrease in the applied stress. The magnitude of the fatigue life cycles under 450 MPa was found to be 1 x 10^5, which increased to 1x10^6 when the applied load was decreased to 250 MPa. The 1 x 10^5 fatigue life cycles that were obtained implies that the as-fabricated Hastelloy-X specimens offered high-cycle fatigue (i.e. fatigue life > 10^4–10^5 cycles) performance, even though the applied stress approached the yield strength. It should be noted that the fatigue life cycles tended to be more scattered with a reduction in the applied stress. Two factors may explain this situation. First, the material was approaching the endurance limit (and thus an asymptote in the S-N curve), which naturally provides some 'spread' in the material's lifetime under constant applied stress. Second, the surface defects and microcracks that were formed during the SLM process are more influential in the low-stress associated with the higher-cycle regions, thus leading to more scattering in that region compared to the higher-stress regions. The dimensions of the samples used for fatigue testing, together with the samples after fatigue testing (250 MPa and 450 MPa) are shown in Fig. 11b.

<insert Figure 11>

Fig. 12 shows SEM micrographs of the fatigue fracture surfaces, which were useful for further fatigue-failure analysis. Fig. 12a 1–3 shows the fracture surface of the specimen under 250 MPa (1.46 x 10^6 cycles; Fig. 11a), while Fig. 13b 1–3 shows the fracture surface of the sample subjected to 450 MPa (1.15 x 10^5 cycles; Fig. 11a). The fracture surfaces of both samples show four distinct regions for structural changes: crack initiation (no number shown), stable crack growth region (I), unstable crack growth region (II) and fracture region (III). (Fig. 12a1, b1.)

<insert Figure 12>

The crack initiation is the early development of fatigue damage that occurs;

the initiation site is generally located at the surface due to the stress concentration and/or surface roughness. Holes were observed in the crack-initiation sites in both samples (Fig. 12a1, b1). Crack initiation occurs because the cyclic slip deformation is not a completely reversible process. Plastic deformation in one direction and then in the reverse direction causes surface ridges and grooves, which suggests that the fatigue process is undergoing stable crack growth (I). With a decrease in applied stress from 450 MPa to 250 MPa, the area of stable crack growth was observed to increase, while both the unstable crack growth and fracture regions were reduced. This situation occurred because the increase in the stable crack growth region (Fig. 12a 1) was correlated to an increase in the length of the main crack, which required an increased number of load cycles, thus increasing the fatigue life (Fig. 11a). In the process of stable crack growth, the rate of the crack growth was found to be very low.

With the number of load cycles continuing, well-defined cracks propagated at a relatively rapid rate, which implies that the fatigue process had entered the unstable crack growth stage. The fatigue structure was observed to offer mixed rupture characteristics; both fatigue striations and secondary cracks were formed during this process (Fig. 12a2, b2). When the crack covered a sufficient area so that the remaining metal at the cross-section could not support the applied load, the sample ruptured by ductile failure (Fig.12a3, b3). It should be noted that the crack propagated from brittle to ductile mode when the fatigue process evolved from the stable to unstable crack growth and fracture regions (Fig. 12a3, b3). In addition, two distinct types of surface areas were observed on the fatigue surface: (1) a smooth surface region caused by the rubbing action between the open surface regions as the crack propagated across the section (region I in Fig. 12a1 and b1) and (2) a rough surface area formed by the fracture when the load became too high for the remaining cross-section (region III in Fig. 12a1 and b1). The unstable crack growth region

(region II) may be regarded as a transition from a smooth to a rough surface. The ductile fatigue fracture surfaces (Fig. 12a3, b3) were observed to offer similar fracture structures to the fracture surfaces generated through tensile testing (Fig. 10a1–3). A dimpled microstructure was observed, and the microcracks that had formed during the SLM were found to have opened considerably.

4. Discussion

4.1. Relative density and laser-working mode

The experimental results demonstrate that laser-energy density strongly affects relative density. When the laser power, layer thickness and hatch spacing are fixed, the laser-energy density is generally inversely proportional to the scanning speed. For instance, when the hatch spacing was maintained at 60 μm (Fig. 2), the laser-energy density increased with the decrease in scanning speed from 800 mm/s to 200 mm/s, while the relative density first increased and then decreased; an optimum 500 mm/s scanning speed was determined. This finding may be attributed to the transition of the laser-working mode between conduction mode and keyhole mode [16]. When the laser-energy density was lower than the threshold (corresponding to 500 mm/s scanning speed), with an increase in energy density – which is generally achieved by reducing the scanning speed – more heat energy could be accumulated, which in turn tended to fully melt the Hastelloy-X powder, thus leading to an increase in relative density. At this stage, the laser works in conduction mode, and the penetration depth is determined by the thermal conductivity of the solidified layers (with scanning speeds of 500–800 mm/s; Fig. 2).

When the laser-energy density goes beyond the threshold, the maximum temperature of the molten pool surface is generally greater than the boiling

point of the powder, which can induce strong evaporation. The recoil pressure that is generated together with Marangoni convection can then cause spattering and depression of the molten pool surface. Keyhole pores and microcracks would then be formed, which would further result in decreases in relative density (scanning speeds of 200–500 mm/s; Fig. 2). This finding is in agreement with [17] and [18], in which the significant effects of recoil pressure and Marangoni convection in the SLM of stainless steel and aluminium nanocomposite were investigated. The experimental results of the present study also imply that the optimum SLM condition (200 mm/s scanning speed and 90 μm hatch spacing) the study determined contributed to a conduction-laser-working mode in the SLM of Hastelloy-X powder. This hypothesis was confirmed by the OM investigation (Fig. 5), in which keyhole pores were not observed in the vertical section.

4.2. Micro-cracks

The experimental results demonstrated that microcracking was the primary defect in the SLM of Hastelloy-X. Under the optimum SLM condition, the porosity was nearly eliminated, while the microcracks were still observed in both the vertical and horizontal sections (Fig. 5). It is well known that thermal residual stress is formed in SLM because of the rapid heating and cooling rates that are used in the process; during the stress relief that occurs through fracturing, if the tensile stress exceeds the ultimate tensile strength of the solid material at a given point and temperature, then microcracks could be formed [19]. Thermally induced cracks are believed to be formed in certain alloys (e.g. nickel super-alloys) during solidification. These cracks cannot be totally eliminated via process optimisation and/or preheating of the plate [3] because the minor alloying elements (e.g. Si) have a strong influence on hot tearing during the solidification process [10]. Harrison et al. [3] proposed that Hastelloy-X's resistance to cracking could be improved by increasing the concentration of substitutional solid solution strengthening atoms within the

lattice.

4.3. Tensile performance

The tensile results demonstrated that the as-fabricated Hastelloy-X in the present work exhibited much better elongation than has been found in the literature [11], in which the elongation of vertically as-fabricated Hastelloy-X was found to be around 30% – much lower than the 40% obtained in this study. This finding may be explained by the laser-energy density induced by the SLM-process parameters this study employed. Compared to the 95 W laser power and 200 mm/s scanning speed used in the present work, Tomus et al. employed a 370 W laser power, 1900 mm/s scanning speed and a 100°C preheated building platform. When the powder layer thickness was taken into consideration, the calculated laser-energy density was 176 J/mm^3 in the present study and 54 J/mm^3 in the literature, respectively. The fairly high elongation (40%) that was observed in the present study also suggests that these vertically fabricated samples were expected to be the least influenced by the microcracks present in both the horizontal and vertical sections.

4.4. Fatigue performance

The fatigue tests demonstrated that the SLM-fabricated Hastelloy-X specimens offered much higher fatigue cycles in the relatively low-cycle range and similar fatigue life in the high-cycle range compared to the CES EduPack [20]. Fig. 13 shows the fatigue performance of Hastelloy-X from the CES database while the stress ratio is maintained at 0.1; the fatigue performance of the SLM-fabricated samples in this study is also indicated. When the applied fatigue strength was 250 MPa, the magnitudes of the fatigue cycles were between 2 x 10^4 and 3 x 10^7 from the CES database, while the fatigue cycles obtained in the present study were between 8 x 10^5 and 1.5 x 10^6 (Fig. 11). When a 300 MPa fatigue strength is chosen, however, the fatigue cycles from

the CES database are between 200 and 4 x 10^4, while the SLM-fabricated specimens offered fatigue cycles between 4 x 10^5 and 8 x 10^5, which are much higher than those of the CES database. With a further increase in the fatigue strength to 350 MPa, the fatigue cycles from the CES database are less than 200, compared to around 3 x 10^5 cycles in the present work. This improved fatigue performance of the SLM-fabricated Hastelloy-X is attributable to the very fine microstructures that were formed during the SLM process. The microcracks that form may have the least influence on the fatigue life of vertically manufactured samples.

<insert Figure 13>

5. Conclusions

This study investigated the microstructure and mechanical properties of as-fabricated Hastelloy-X using the selective laser melting (SLM) process. The fatigue performance in particular was systematically examined for the first time in this work. This paper has presented the following important findings derived from the experimental results.

(1) An optimum 200 mm/s scanning speed and 90 μm hatch spacing were determined by quantifying the relative density of the as-fabricated cubic samples (10 x 10 x 10 mm) using the Archimedes method. The relative density was found to be as high as 99.5% under the optimum process parameters.

(2) The primary defect in the as-fabricated Hastelloy-X was microcracks instead of pores, because the minor alloying elements (e.g. Si) have a strong influence on hot tearing during the solidification process. The XRD patterns indicated that the austenite single phase was formed, with an FCC crystal structure. Due to the difference in solidification rates, the microstructure offered different types of grain orientations.

(3) A consistent 470 MPa yield strength with a very high elongation of 40% was achieved in the study; the elongation that was obtained was much higher than the previously reported 30%. The cracks that formed may have had the least tensile influence on the vertically fabricated specimens, although the microcracks were observed to have been greatly opened at the fracture surface.

(4) The fatigue performance of SLM-fabricated Hastelloy-X was systematically investigated for the first time in this study. Compared to the available CES EduPack, the SLM-manufactured samples exhibited much higher fatigue life in relatively low-cycle ranges and a similar fatigue life in high-cycle ranges.

The mechanism of the microcrack formation and post-process (e.g. hot isostatic pressing [HIP]) require further investigation to eliminate these defects. Therefore, in order to obtain a better understanding of the SLM of Hastelloy-X used in gas turbine engines, machine manufacturers and academic researchers should ideally work together to provide a feasible solution.

Acknowledgement

The authors would like to thank Dr. Sasan Dadbakhsh and Mr. Haiyang Fan from KU Leuven for the valuable discussions and SEM operations. The lead author (Quanquan Han) gratefully appreciates the financial support of Cardiff University–KU Leuven Research Collaboration Funding.

References

[1] H.U. Hong, I.S. Kim, B.G. Choi, H.W. Jeong, C.Y. Jo, Effects of temperature and strain range on fatigue cracking behavior in Hastelloy X, Mater. Lett. 62 (2008) 4351–4353. doi:10.1016/j.matlet.2008.07.032.

[2] J.C. Zhao, M. Larsen, V. Ravikumar, Phase precipitation and time-temperature-transformation diagram of Hastelloy X, Mater. Sci. Eng. A. 293 (2000) 112–119. doi:10.1016/S0921-5093(00)01049-2.

[3] N.J. Harrison, I. Todd, K. Mumtaz, Reduction of micro-cracking in nickel superalloys processed by Selective Laser Melting: A fundamental alloy design approach, Acta

Mater. 94 (2015) 59–68. doi:10.1016/j.actamat.2015.04.035.

[4] Q. Han, R. Setchi, S.L. Evans, Synthesis and characterisation of advanced ball-milled Al-Al_2O_3 nanocomposites for selective laser melting, Powder Technol. 297 (2016) 183–192. doi:10.1016/j.powtec.2016.04.015.

[5] Q. Han, Y. Geng, R. Setchi, F. Lacan, D. Gu, S.L. Evans, Macro and nanoscale wear behaviour of Al-Al_2O_3 nanocomposites fabricated by selective laser melting, Compos. Part B Eng. 127 (2017) 26–35. doi:10.1016/j.compositesb.2017.06.026.

[6] F. Wang, X.H. Wu, D. Clark, On direct laser deposited Hastelloy X: dimension, surface finish, microstructure and mechanical properties, Mater. Sci. Technol. 27 (2011) 344–356. doi:10.1179/026708309X12578491814591.

[7] P. Zhang, Z. Zhang, L. Li, Z. Zhang, Twin boundary: Stronger or weaker interface to resist fatigue cracking, Scr. Mater. 66 (2012) 854–859. doi:10.1016/j.scriptamat.2012.01.028.

[8] D. Tomus, T. Jarvis, X. Wu, J. Mei, P. Rometsch, E. Herny, J.F. Rideau, S. Vaillant, Controlling the microstructure of Hastelloy-X components manufactured by Selective Laser Melting, Phys. Procedia. 41 (2013) 823–827. doi:10.1016/j.phpro.2013.03.154.

[9] L.N. Carter, X. Wang, N. Read, R. Khan, M. Aristizabal, K. Essa, M.M. Attallah, Process optimisation of selective laser melting using energy density model for nickel based superalloys, Mater. Sci. Technol. 32 (2016) 657–661. doi:10.1179/1743284715Y.0000000108.

[10] D. Tomus, P.A. Rometsch, M. Heilmaier, X. Wu, Effect of minor alloying elements on crack-formation characteristics of Hastelloy-X manufactured by selective laser melting, Addit. Manuf. 16 (2017) 65–72. doi:10.1016/j.addma.2017.05.006.

[11] D. Tomus, Y. Tian, P.A. Rometsch, M. Heilmaier, X. Wu, Influence of post heat treatments on anisotropy of mechanical behaviour and microstructure of Hastelloy-X parts produced by selective laser melting, Mater. Sci. Eng. A. 667 (2016) 42–53. doi:10.1016/j.msea.2016.04.086.

[12] T. Etter, K. Kunze, F. Geiger, H. Meidani, Reduction in mechanical anisotropy through high temperature heat treatment of Hastelloy X processed by Selective Laser Melting (SLM), IOP Conf. Ser. Mater. Sci. Eng. 82 (2015) 012097. doi:10.1088/1757-899X/82/1/012097.

[13] Y. Tian, D. Tomus, P. Rometsch, X. Wu, Influences of processing parameters on surface roughness of Hastelloy X produced by selective laser melting, Addit. Manuf. 13 (2017) 103–112. doi:10.1016/j.addma.2016.10.010.

[14] F. Wang, Mechanical property study on rapid additive layer manufacture Hastelloy X alloy by selective laser melting technology, Int. J. Adv. Manuf. Technol. 58 (2012) 545–551. doi:10.1007/s00170-011-3423-2.

[15] L. Thijs, F. Verhaeghe, T. Craeghs, J. Van Humbeeck, J.P. Kruth, A study of the microstructural evolution during selective laser melting of Ti-6Al-4V, Acta Mater. 58 (2010) 3303–3312. doi:10.1016/j.actamat.2010.02.004.

[16] W.E. King, H.D. Barth, V.M. Castillo, G.F. Gallegos, J.W. Gibbs, D.E. Hahn, C. Kamath, A.M. Rubenchik, Observation of keyhole-mode laser melting in laser powder-bed fusion additive manufacturing, J. Mater. Process. Technol. 214 (2014) 2915–2925. doi:10.1016/j.jmatprotec.2014.06.005.

[17] S.A. Khairallah, A.T. Anderson, A. Rubenchik, W.E. King, Laser powder-bed fusion additive manufacturing: Physics of complex melt flow and formation mechanisms of pores, spatter, and denudation zones, Acta Mater. 108 (2016) 36–45. doi:10.1016/j.actamat.2016.02.014.

[18] Q. Han, R. Setchi, F. Lacan, D. Gu, S.L. Evans, Selective laser melting of advanced Al-Al_2O_3 nanocomposites: Simulation, microstructure and mechanical properties, Mater. Sci. Eng. A. 698 (2017) 162–173. doi:10.1016/j.msea.2017.05.061.

[19] P. Mercelis, J.P. Kruth, Residual stresses in selective laser sintering and selective laser melting, Rapid Prototyp. J. 12 (2006) 254–265. doi:10.1108/13552540610707013.

[20] CES Selector Software, Granta Design Limited, Cambridge, UK. www.grantadesign.com (accessed September 1, 2017).

Figures

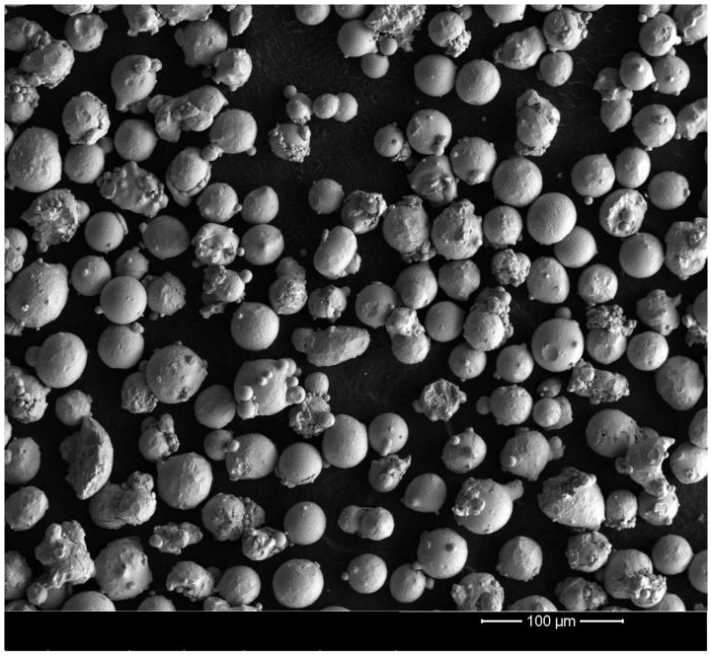

Fig.1. Morphology of raw Hastelloy-X.

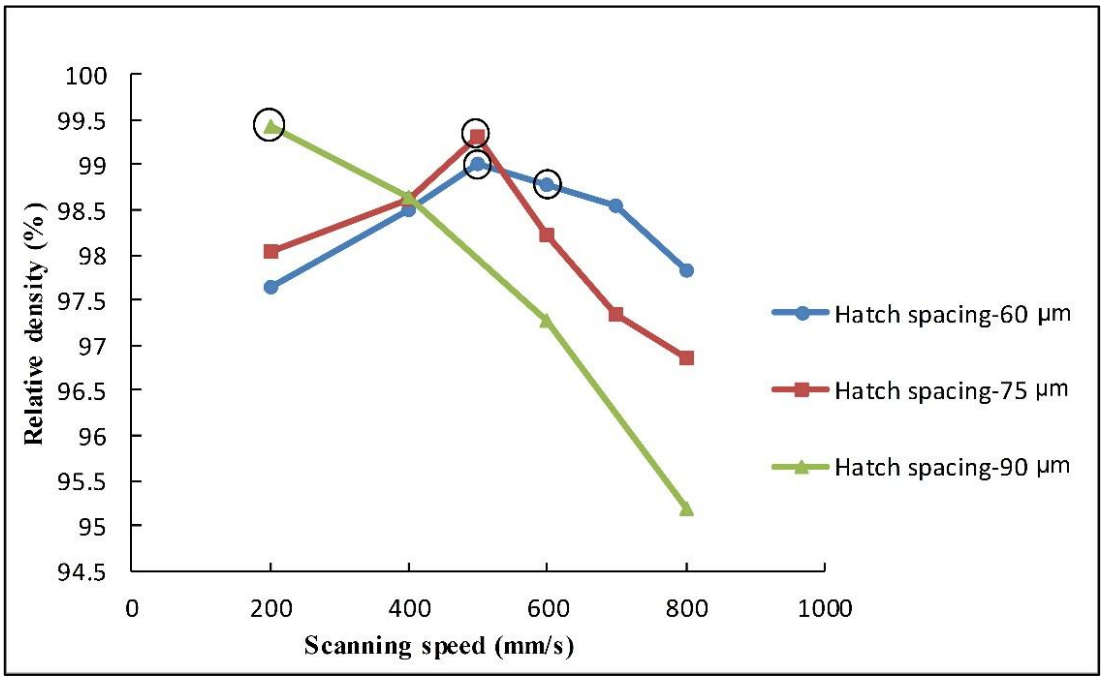

Fig.2. Relative density of the as-fabricated samples.

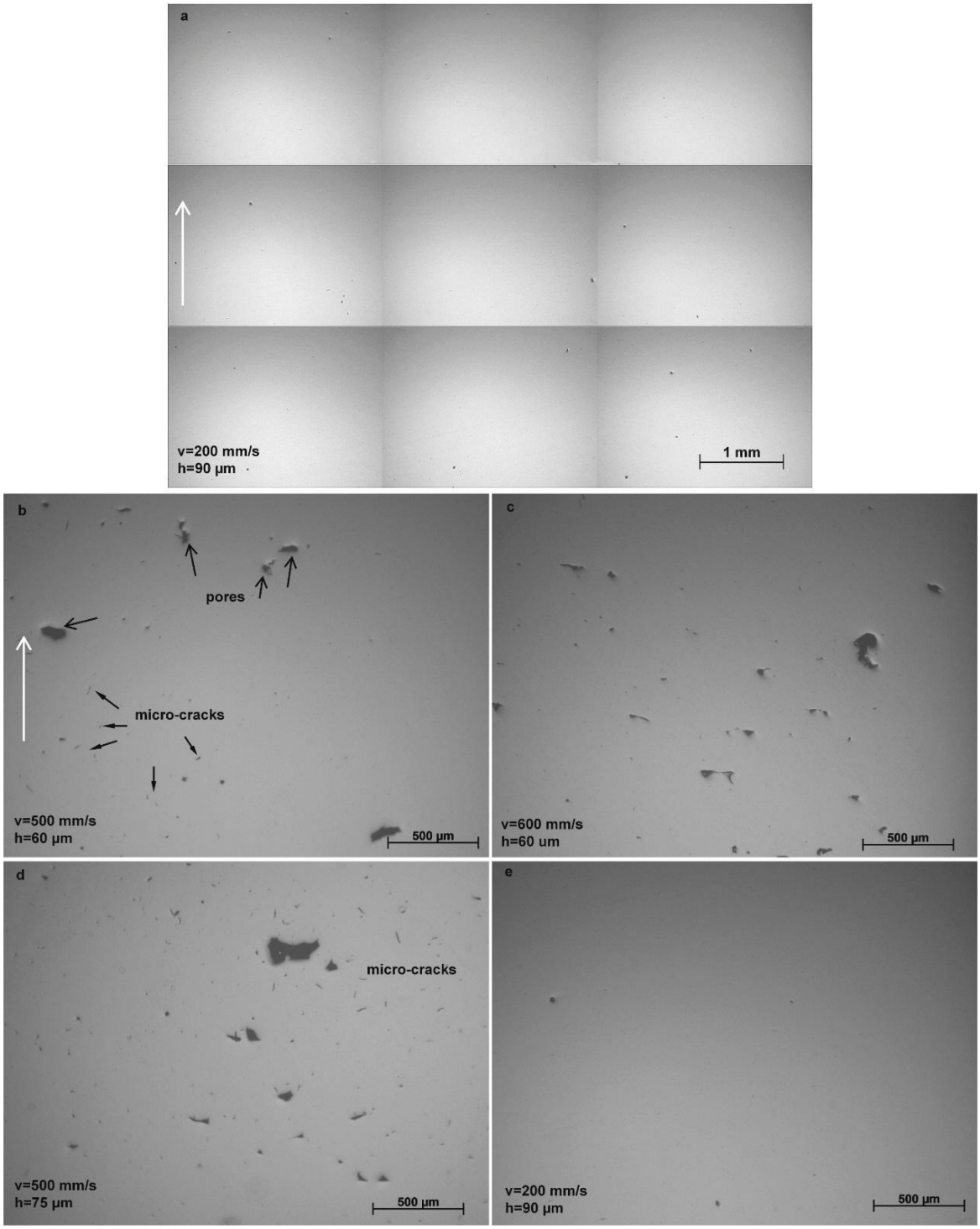

Fig. 3. OM images showing porosity and cracks in the vertical sections under different conditions: (a) elongated sample at 200mm/s, 90 µm; (b) 500 mm/s, 60 µm; (c) 600 mm/s, 60 µm; (d) 500 mm/s, 75 µm and (e) 200 mm/s, 90 µm; the white arrow indicates the building direction.

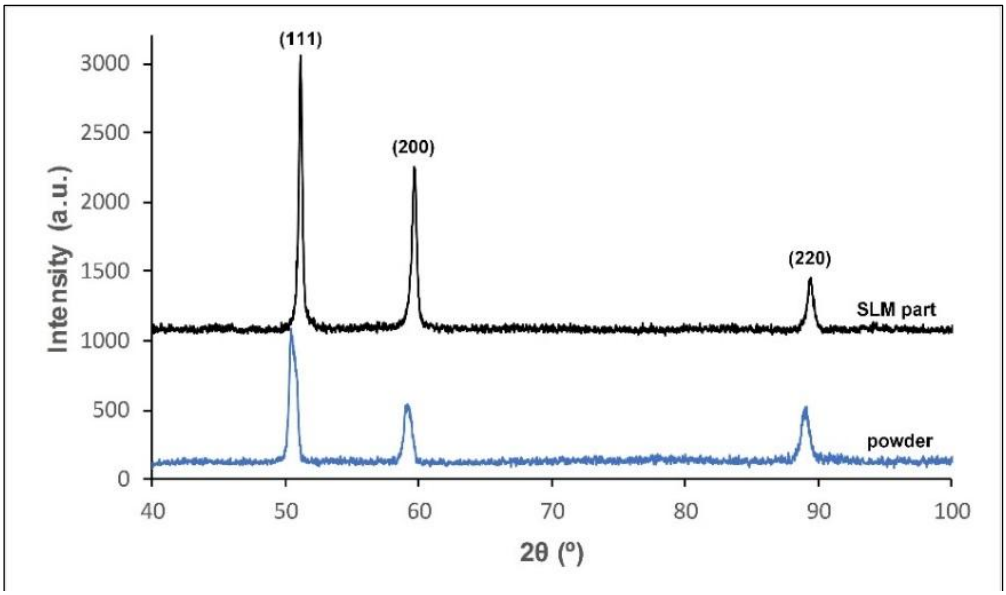

Fig. 4. XRD patterns of the Hastelloy-X powder and SLM-fabricated part.

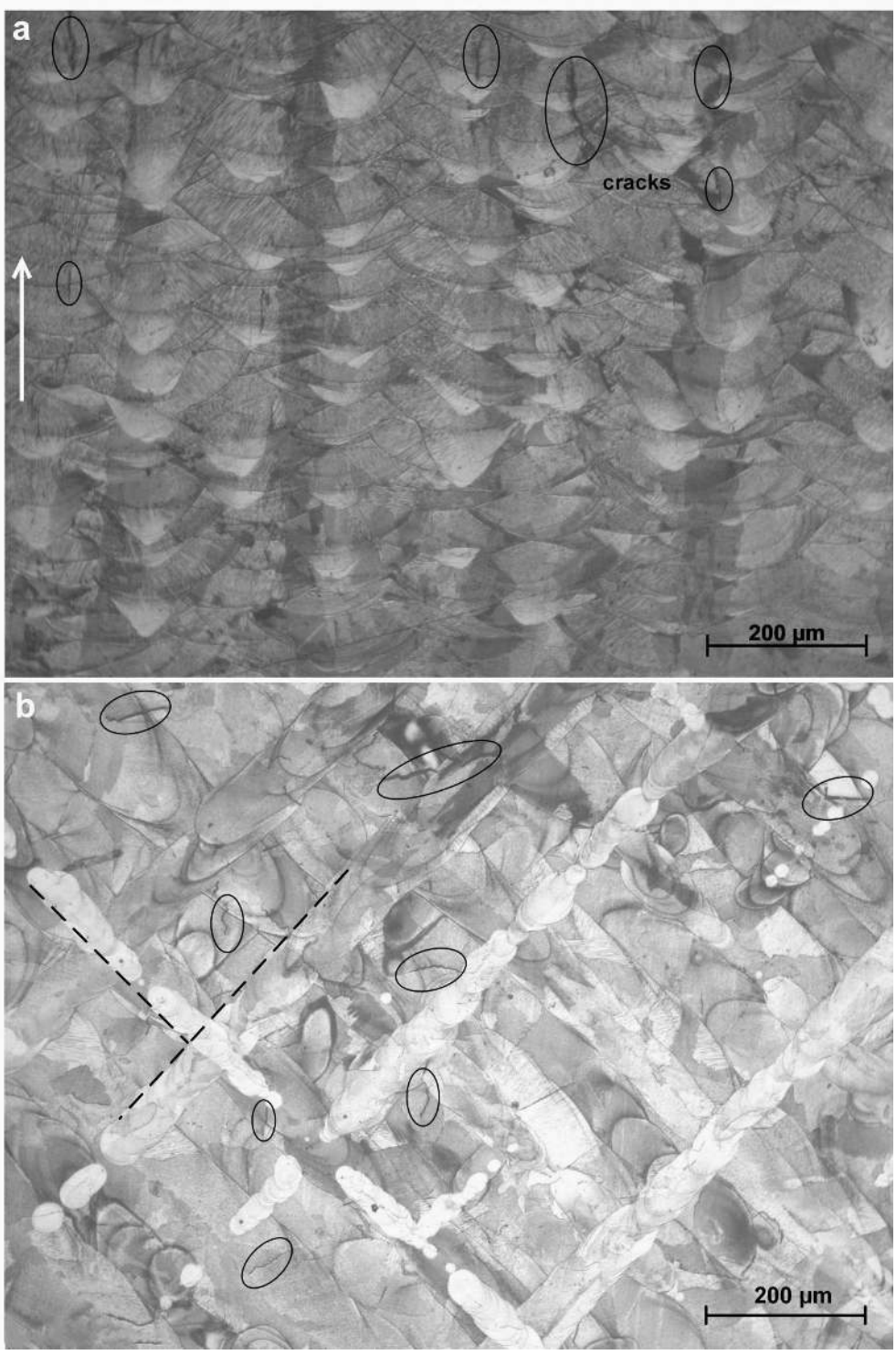

Fig. 5. OM images showing the microstructure of (a) vertical and (b) horizontal sections fabricated at a scanning speed of 200 mm/s and hatch spacing of 90 µm; the white arrow indicates the building direction.

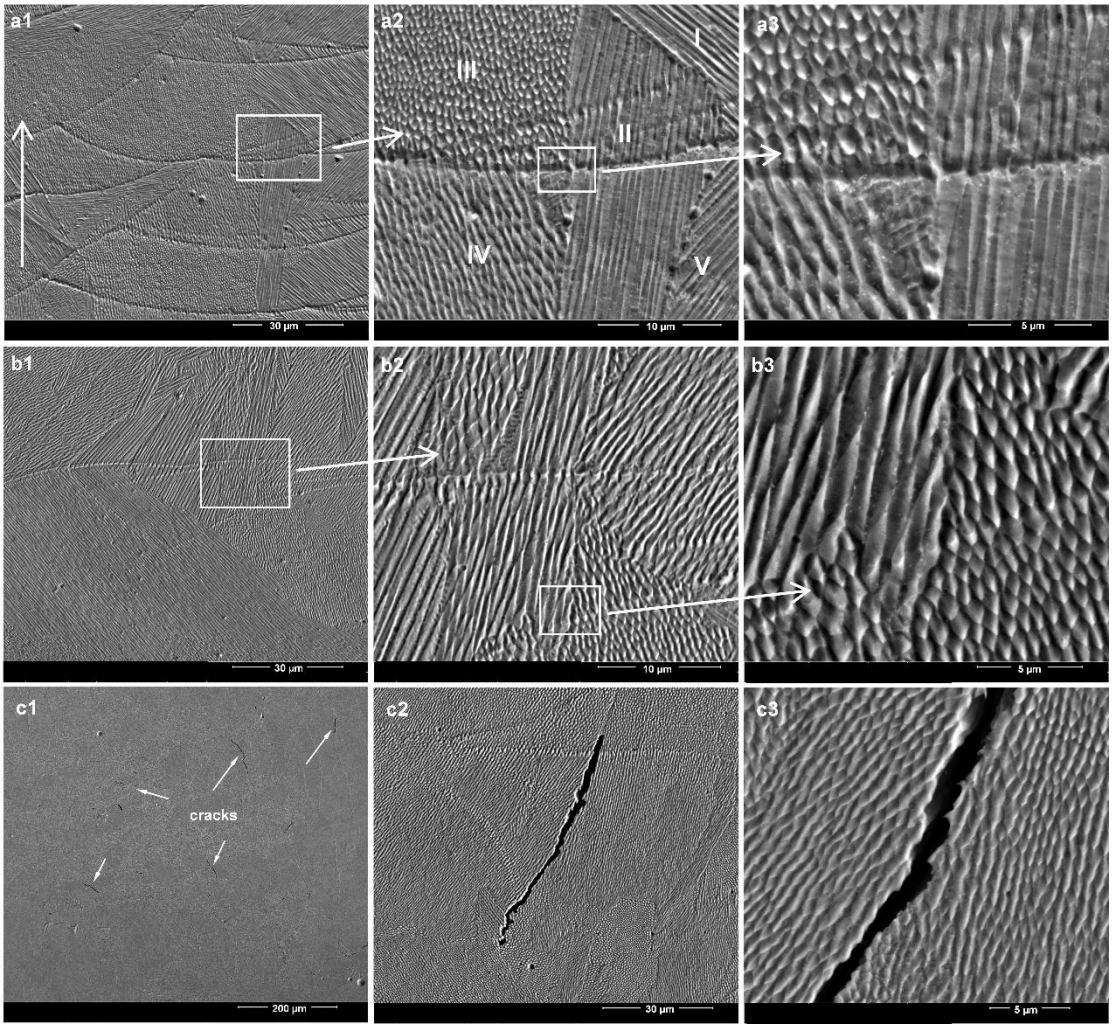

Fig. 6. SEM images showing the microstructures of vertical and horizontal sections fabricated under the optimum parameters: (a1–a3) vertical section (regions I–V presented different types of solidification microstructures); (b1–b3) horizontal section; (c1–c3) microcracks observed on the horizontal section.

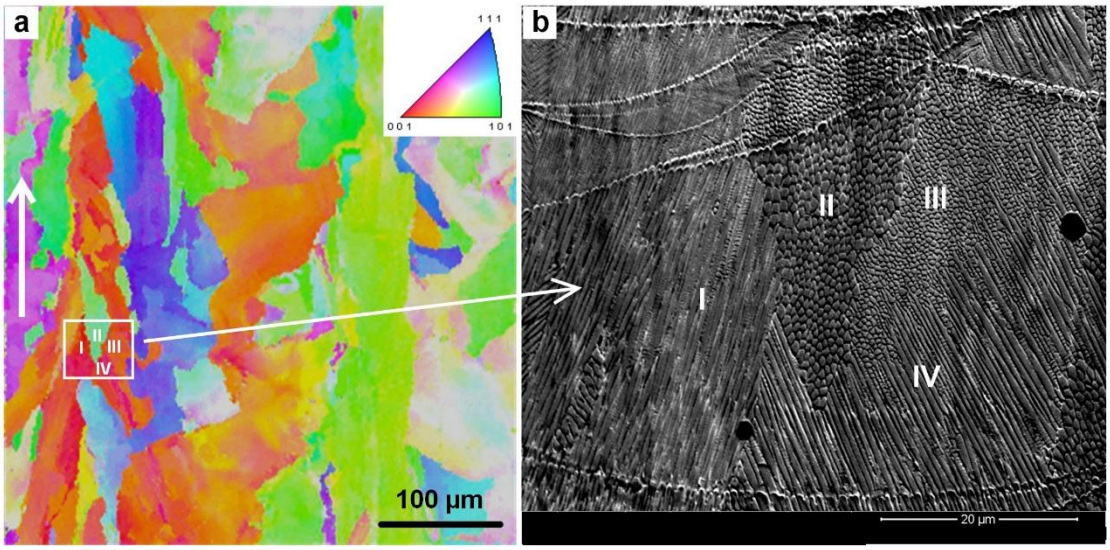

Fig. 7. EBSD orientation map of the vertical section; the arrow indicates the building direction.

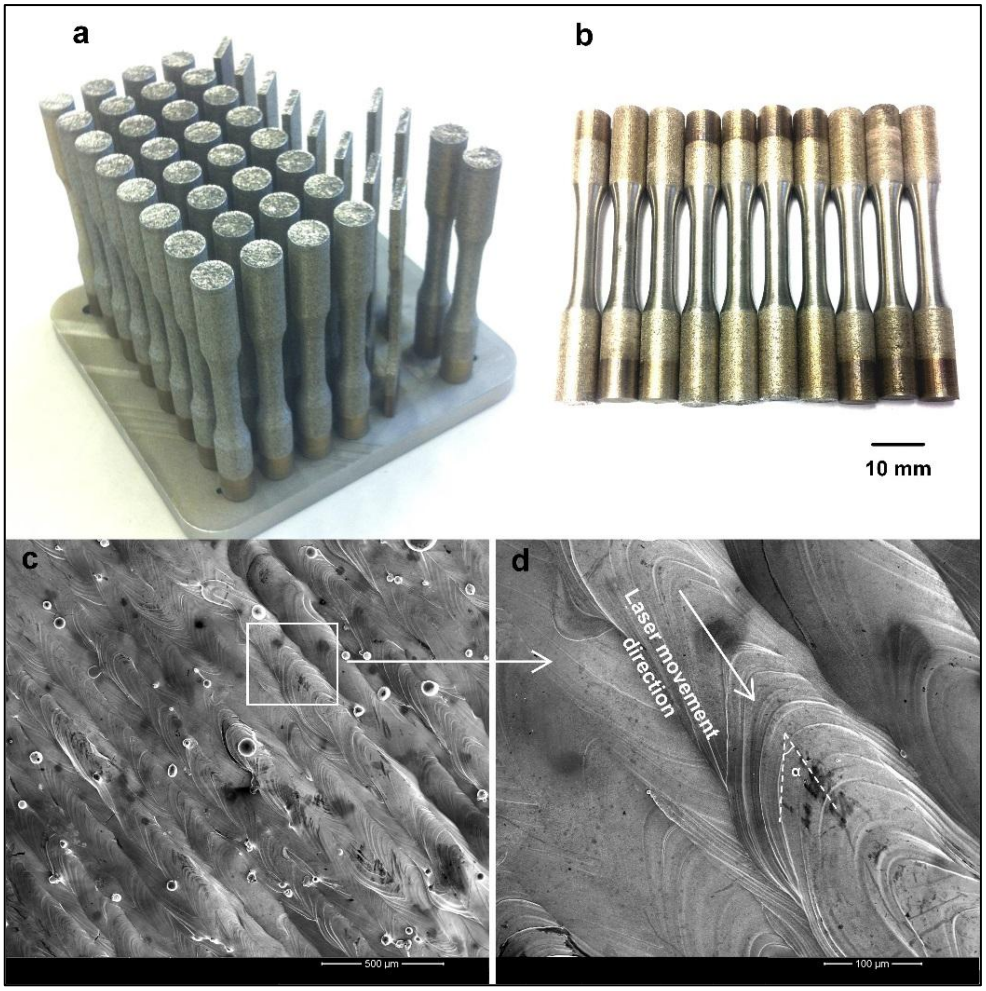

Fig. 8. Images showing the fabricated tensile and fatigue specimens (a–b) and specimen top-surface topography fabricated under optimum parameters (c–d).

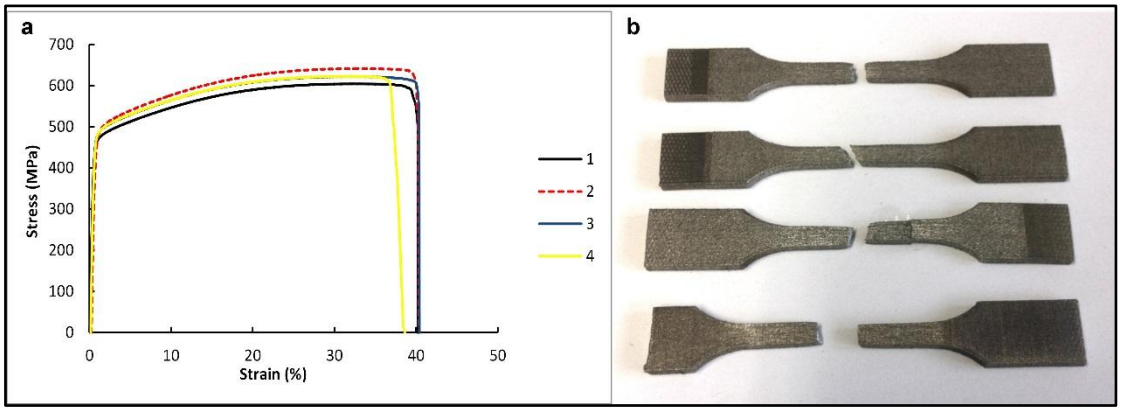

Fig. 9. Tensile performance of the as-fabricated Hastelloy-X samples.

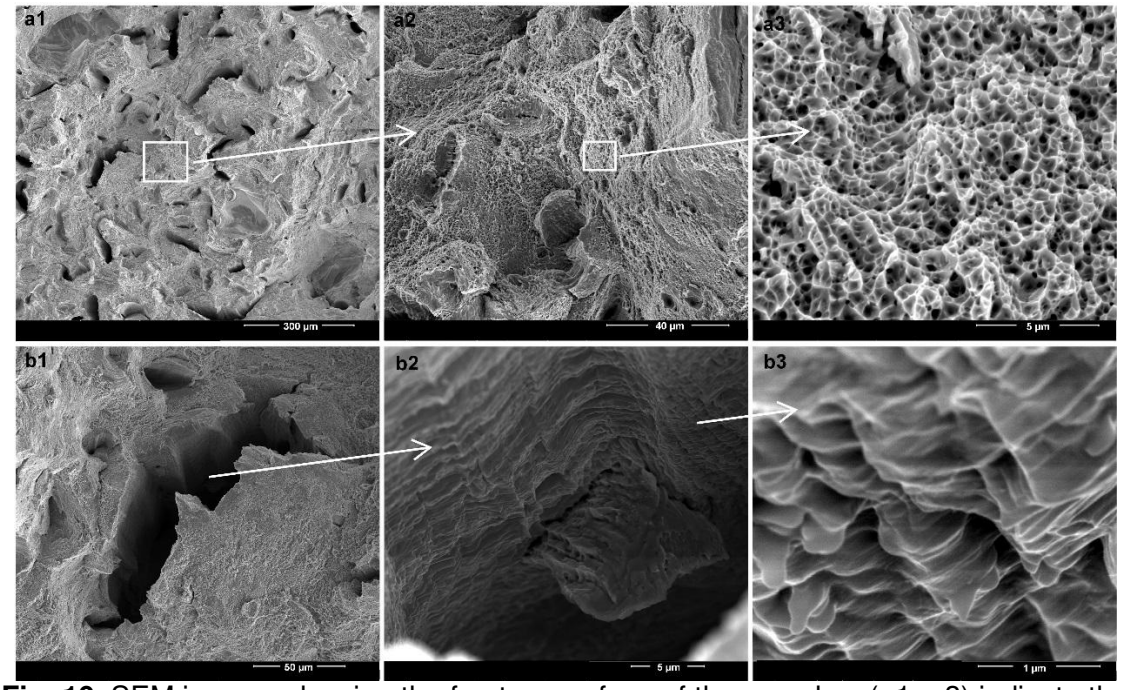

Fig. 10. SEM images showing the fracture surface of the samples: (a1–a3) indicate the ductile fracture and (b1–b3) show the morphology of the microcracking.

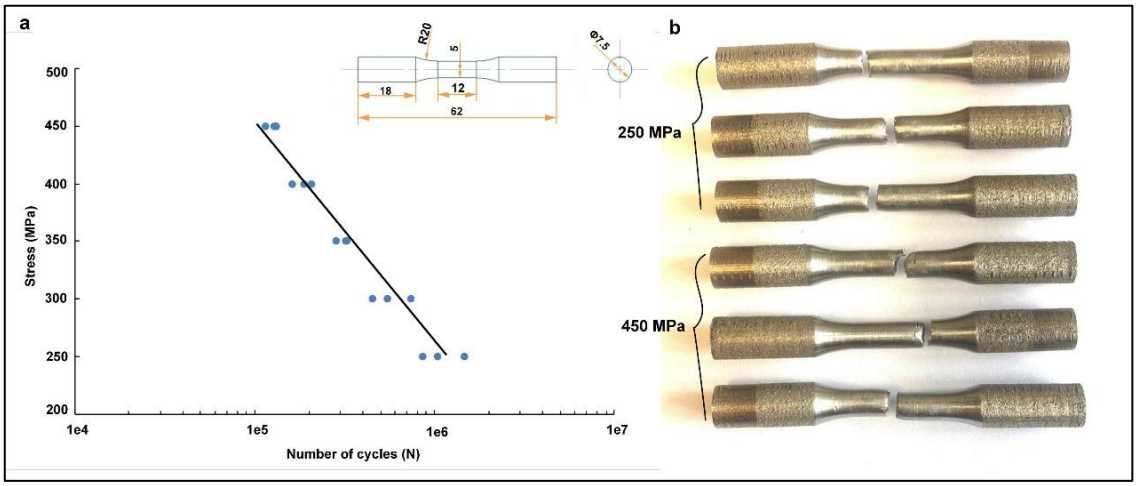

Fig. 11. (a) Fatigue performance of the as-fabricated Hastelloy-X samples; (b) photograph of the samples after the fatigue testing.

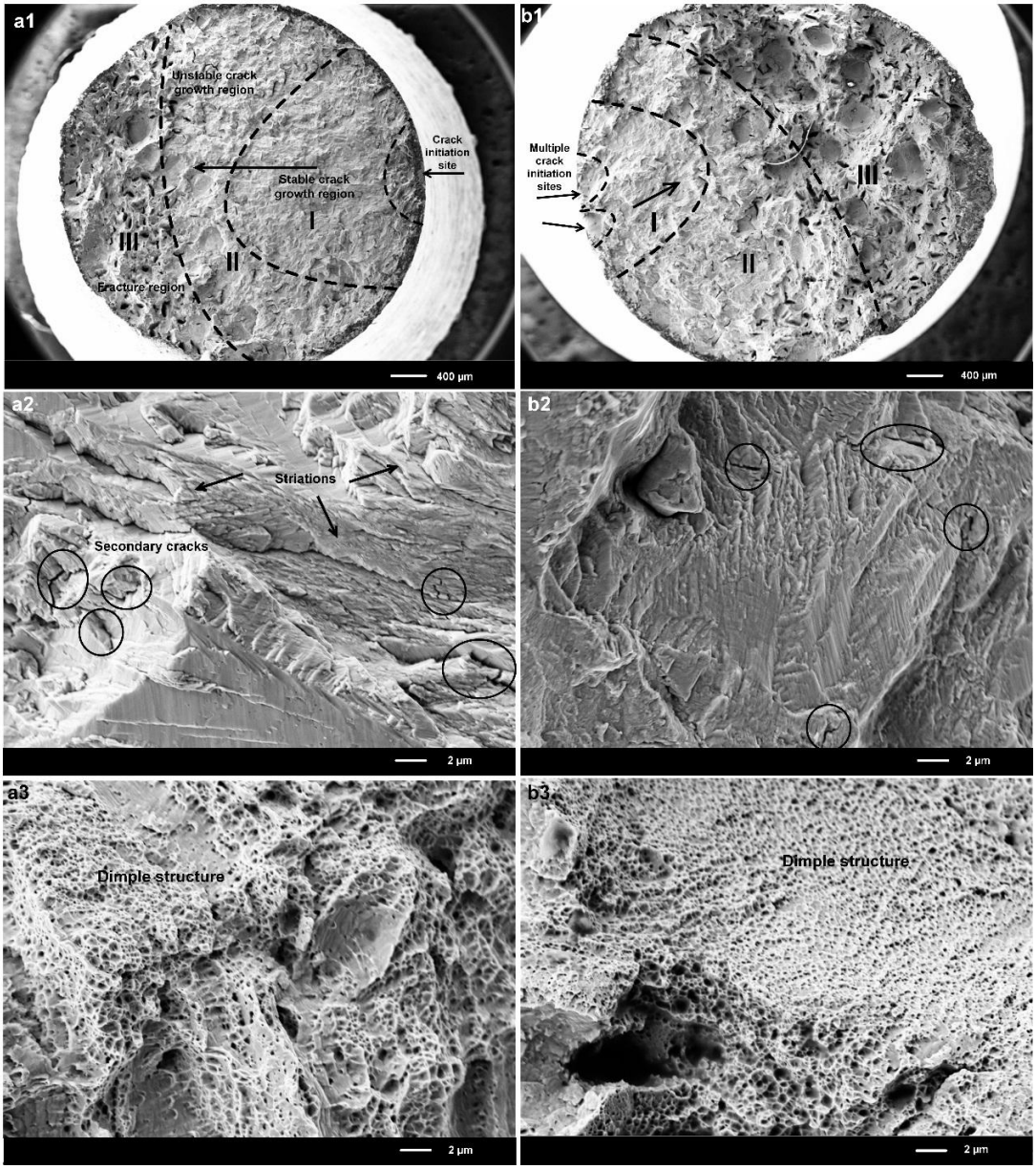

Fig. 12. SEM micrographs showing fatigue-fracture surfaces under the stress of 250 MPa (a1–a3) and 450 MPa (b1–b3).

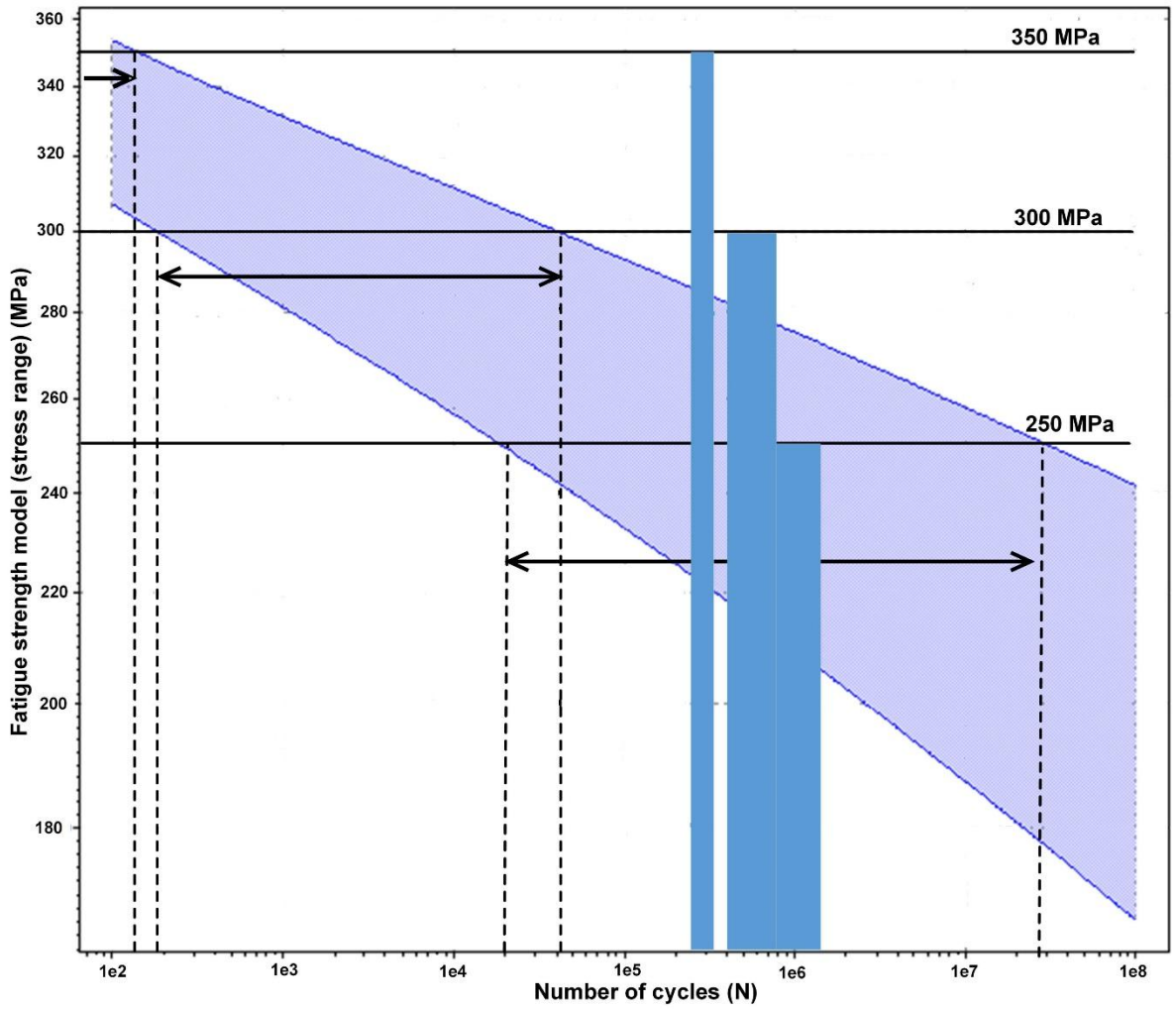

Fig. 13. Fatigue performance of Hastelloy-X from the CES database [20] (blue bars showing the obtained fatigue life in present study)**.**

Tables

Table 1

Process parameters.

Parameter	Value	Parameter	Value
Laser power (W)	95	Scanning speed (mm/s)	200–800
Beam diameter (μm)	50	Hatch spacing (μm)	60, 75, 90
Layer thickness (μm)	30	Scanning strategy	Bidirectional scanning with a 90º rotation between layers

Table 2.

Properties from tensile tests

Young's modulus (GPa)	Yield strength (MPa)	Ultimate tensile strength (MPa)	Elongation (%)
149±9	470±10	623±15	40±1